

ANTENNA PATTERN CONTROL USING IMPEDANCE SURFACES

Semiannual Progress Report

Constantine A. Balanis and Kefeng Liu

September 16, 1991 – March 15, 1992

Telecommunications Research Center
Department of Electrical Engineering
Arizona State University
Tempe, Arizona 85287-7206

Grant No. NAG-1-1183
National Aeronautics and Space Administration
AVRADA Joint Research Program Office
Langley Research Center
Hampton, VA 23665

ABSTRACT

This is a semiannual progress report for the *Antenna Pattern Control Using Impedance Surfaces* research grant. This report covers the research period from September 16, 1991 to March 15, 1992.

During this research period, some modifications of the moment method code were made. Analyses of horn antennas have been conducted extensively. Excellent agreements with measured results have been observed for pyramidal horn antennas with perfectly conducting surfaces. The predicted results are so accurate that even the finest ripple structures in the far-field radiation patterns are computed correctly. Preliminary results for the radiating patterns of pyramidal horns with impedance surfaces were also obtained. Discussions of using the code in accurate modeling of practical pyramidal horn antennas are also included. After the code for the analysis of the horn antennas with impedance materials is finalized, the synthesis problem will be examined in the coming research period.

I. INTRODUCTION

A. Modification of the Code

In previous reporting periods, we presented the stepped-waveguide and hybrid field integral equation method for the analysis of horn antenna. To make the code more adaptable to the analysis of pyramidal horn antennas with impedance walls, TM_y and TE_y (instead of TM_z and TE_z) modes are chosen to represent the fields in the stepped-waveguide section. The transition equations relating full-wave coefficients on both sides of the stepped junction are given by (see also page 6 of our September 16, 1990–March 15, 1991 report)

$$A_{mn}^{(2)} + B_{mn}^{(2)} = \sum_{kl} \frac{\omega^2 \mu \epsilon - \beta_y^{(1)2}}{\omega^2 \mu \epsilon - \beta_y^{(2)2}} (A_{kl}^{(1)} + B_{kl}^{(1)}) U_{mnkl} \quad (1)$$

$$\begin{aligned} C_{mn}^{(2)} + D_{mn}^{(2)} &= \sum_{kl} \frac{\omega \mu \beta_x^{(2)} (\beta_y^{(2)2} - \beta_y^{(1)2})}{\beta_z^{(2)} \beta_y^{(2)} (\omega^2 \mu \epsilon - \beta_y^{(2)2})} U_{mnkl} (A_{kl}^{(1)} + B_{kl}^{(1)}) \\ &+ \sum_{kl} \frac{\beta_z^{(1)}}{\beta_z^{(2)}} V_{mnkl} (C_{kl}^{(1)} + D_{kl}^{(1)}) \end{aligned} \quad (2)$$

$$\begin{aligned} A_{kl}^{(1)} - B_{kl}^{(1)} &= \sum_{mn} \frac{\beta_z^{(2)}}{\beta_z^{(1)}} U_{mnkl} (A_{mn}^{(2)} - B_{mn}^{(2)}) \\ &+ \sum_{mn} \frac{\omega \epsilon \beta_x^{(2)} (\beta_y^{(2)2} - \beta_y^{(1)2})}{\beta_z^{(1)} \beta_y^{(2)} (\omega^2 \mu \epsilon - \beta_y^{(1)2})} U_{mnkl} (C_{mn}^{(2)} - D_{mn}^{(2)}) \end{aligned} \quad (3)$$

$$C_{kl}^{(1)} - D_{kl}^{(1)} = \sum_{mn} \frac{\omega^2 \mu \epsilon - \beta_y^{(2)2}}{\omega^2 \mu \epsilon - \beta_y^{(1)2}} (C_{mn}^{(2)} - D_{mn}^{(2)}) V_{mnkl} \quad (4)$$

This choice of eigen expansion gives more weights to the few dominant TM_y modes to represent the field distributions. Therefore, the numerical process of combining scattering matrices is more robust. Unfortunately, this representation also has

its setback. The problem is that the factor $\omega^2\mu\epsilon - \beta_y^2$ appears in both the numerator and denominator in the transition equations. In a rare occasion, this factor can approach to zero, causing numerical difficulties. The 7-inch square horns presented in our March 16,1991–September 15, 1991 report happens to encounter such an occasion on the radiation aperture for some of the modes. The error caused by this was partially responsible for the excessive differences between the measured and the predicted results presented in the report. We discovered this problem in the problem in the early stage of this reporting period, and the alternative TM_z and TE_z modes were chosen to replace TM_y and TE_y modes. An outline of the differences in the transition equations in the two sets of eigen mode expansions are presented here.

When TM_z and TE_z modes are chosen to represented the electromagnetic fields in the waveguide sections, the two z component vector potentials (A_z and F_z) can expressed as

$$F_z = \epsilon \sum_{\substack{m=1,M \\ n=0,N}} (A_{mn}e^{-j\beta_z z} + B_{mn}e^{j\beta_z z})C_{mn}(x,y) \quad (5)$$

$$A_z = \sqrt{\mu\epsilon} \sum_{\substack{m=1,M \\ n=2,N}} (C_{mn}e^{-j\beta_z z} - D_{mn}e^{j\beta_z z})P_{mn}(x,y) \quad (6)$$

$$\beta_z = \sqrt{\omega^2\mu\epsilon - \beta_x^2 - \beta_y^2} \quad (7)$$

$$C_{mn}(x,y) = \frac{2 \cos(\beta_x x) \cos(\beta_y y)}{\beta_c \sqrt{ab}(1 + \delta_{no})}$$

$$P_{mn}(x,y) = \frac{2 \sin(\beta_x x) \sin(\beta_y y)}{\beta_c \sqrt{ab}} \quad (8)$$

$$\beta_c = \sqrt{\beta_x^2 + \beta_y^2} \quad (9)$$

Then the transverse electric and magnetic fields due to the two vector potentials can be found by the following equations[1]:

$$E_x = -\frac{1}{\epsilon} \frac{\partial F_z}{\partial y} - j \frac{1}{\omega \mu \epsilon} \frac{\partial^2 A_z}{\partial x \partial z} \quad (10)$$

$$E_y = \frac{1}{\epsilon} \frac{\partial F_z}{\partial x} - j \frac{1}{\omega \mu \epsilon} \frac{\partial^2 A_z}{\partial y \partial z} \quad (11)$$

$$H_x = -j \frac{1}{\omega \mu \epsilon} \frac{\partial^2 F_z}{\partial x \partial z} + \frac{1}{\mu} \frac{\partial A_z}{\partial y} \quad (12)$$

$$H_y = -j \frac{1}{\omega \mu \epsilon} \frac{\partial^2 F_z}{\partial y \partial z} - \frac{1}{\mu} \frac{\partial A_z}{\partial x} \quad (13)$$

On the stepped-waveguide junction, the boundary conditions relating the two waveguides are

$$E_{x,y}^{(1)}(x, y)|_{on A} = E_{x,y}^{(2)}(x, y)|_{on A} \quad (14)$$

$$E_{x,y}^{(2)}(x, Y)|_{on \Delta A} = 0 \quad (15)$$

$$H_{x,y}^{(1)}(x, y)|_{on A} = H_{x,y}^{(2)}(x, y)|_{on A} \quad (16)$$

where A is the area of the smaller waveguide section, and ΔA is the ring area of the larger waveguide section extracting A . The boundary conditions in (14)-(16) uniquely define the relation between the full-wave expansion coefficients on both sides of the junction. The resulting transition equations for TM_z and TE_z are given by

$$A_{mn}^{(2)} + B_{mn}^{(2)} = \sum_{kl} \frac{\beta_c^{(1)} \beta_x^{(2)}}{\beta_c^{(2)} \beta_x^{(1)}} U_{mnkl} (A_{kl}^{(1)} + B_{kl}^{(1)}) \quad (17)$$

$$C_{mn}^{(2)} + D_{mn}^{(2)} = \sum_{kl} \frac{\beta_o [(\beta_x^{(1)} \beta_y^{(2)})^2 - (\beta_x^{(2)} \beta_y^{(1)})^2]}{\beta_z^{(2)} \beta_x^{(1)} \beta_y^{(2)} \beta_c^{(2)} \beta_c^{(1)}} U_{mnkl} (A_{kl}^{(1)} + B_{kl}^{(1)})$$

$$+ \sum_{kl} \frac{\beta_x^{(1)} \beta_c^{(2)} \beta_z^{(1)}}{\beta_x^{(2)} \beta_c^{(1)} \beta_z^{(2)}} V_{mnkl} (C_{kl}^{(1)} + D_{kl}^{(1)}) \quad (18)$$

$$\begin{aligned} A_{kl}^{(1)} - B_{kl}^{(1)} &= \sum_{mn} \frac{\beta_z^{(2)} \beta_c^{(1)} \beta_x^{(2)}}{\beta_z^{(1)} \beta_c^{(2)} \beta_x^{(1)}} U_{mnkl} (A_{mn}^{(2)} - B_{mn}^{(2)}) \\ &+ \sum_{mn} \frac{\beta_o [(\beta_x^{(1)} \beta_y^{(2)})^2 - (\beta_x^{(2)} \beta_y^{(1)})^2]}{\beta_z^{(1)} \beta_x^{(1)} \beta_y^{(2)} \beta_c^{(2)} \beta_c^{(1)}} U_{mnkl} (C_{mn}^{(2)} - D_{mn}^{(2)}) \end{aligned} \quad (19)$$

$$C_{kl}^{(1)} - D_{kl}^{(1)} = \sum_{mn} \frac{\beta_x^{(1)} \beta_c^{(2)}}{\beta_x^{(2)} \beta_c^{(1)}} V_{mnkl} (C_{mn}^{(2)} - D_{mn}^{(2)}) \quad (20)$$

where

$$U_{mnkl} = \frac{4 \int_0^{a_1} \int_0^{b_1} \sin(\beta_x^{(2)} x') \sin(\beta_x^{(1)} x) \cos(\beta_y^{(2)} y') \cos(\beta_y^{(1)} y) dx dy}{\sqrt{a_1 a_2 b_1 b_2} (1 + \delta_{no}) (1 + \delta_{lo})} \quad (21)$$

$$V_{mnkl} = \frac{4 \int_0^{a_1} \int_0^{b_1} \cos(\beta_x^{(2)} x') \cos(\beta_x^{(1)} x) \sin(\beta_y^{(2)} y') \sin(\beta_y^{(1)} y) dx dy}{\sqrt{a_1 a_2 b_1 b_2}} \quad (22)$$

$$x' = x + \frac{\Delta a}{2} = x + \frac{a_2 - a_1}{2} \quad (23)$$

$$y' = y + \frac{\Delta b}{2} = y + \frac{b_2 - b_1}{2} \quad (24)$$

The integrals in U_{mnkl} and V_{mnkl} can be performed analytically and reduced to

$$U_{mnkl} = \frac{4[1 + (-1)^{m+k}][1 + (-1)^{n+l}]}{\sqrt{a_1 a_2 b_1 b_2} (1 + \delta_{no}) (1 + \delta_{lo})} \frac{\beta_x^{(1)} \sin(\beta_x^{(2)} \frac{\Delta a}{2})}{\beta_x^{(1)2} - \beta_x^{(2)2}} \frac{\beta_y^{(2)} \sin(\beta_y^{(1)} \frac{\Delta b}{2})}{\beta_y^{(1)2} - \beta_y^{(2)2}} \quad (25)$$

$$V_{mnkl} = \frac{\beta_x^{(2)} \beta_y^{(1)}}{\beta_x^{(1)} \beta_y^{(2)}} U_{mnkl} \quad (26)$$

In the transition equations (17)–(20), the only possible factor to have singular value is β_z . This singular value occurs less frequently and is having a weaker singularity because of the square root operation in (7). This singularity can be easily avoided in the middle of the transition by varying the stepped size by a small value.

On the radiation aperture, it can be numerically treated with better accuracy than in TM_y and TE_y case because of the weaker singularity. Therefore, the transition computed by this formulations is much more stable in accuracy for any configuration of horn transitions.

B. Higher Order Modes

One of the reason for the inaccuracy of the predicted patterns (Figures 7 to 10) presented in the previous reporting period is because there were not enough higher order modes included in the computation of the horn transition and in the aperture discontinuity. We realized this problem in this research period, and the following were measures taken to determine the number of higher order modes.

Pyramidal horns are generally excited by the dominant TE_{10} mode from the feeding waveguide, and higher order of TE_{mn} and TM_{mn} modes are generated in the transition. For the pyramidal horn with symmetrical flarings on both dimensions, only those modes which have $m = 1, 3, 5, 7, \dots, M$ and $n = 0$ (for TE modes only), $2, 4, 6, \dots, N$ are generated in the transition. The couplings between TE_{mn} and TM_{mn} modes are analytically calculated by (17)-(20). There are two factors which affect the accuracy of the stepped waveguide modeling of the continuous horn transition: the size of the stepped discontinuity in modeling the continuous horn transition with a finite number of cascaded stepped waveguides, and the required highest order modes (M and N) in (5)-(6). Our experience demonstrates that good accuracy can be achieved by limiting the maximum size of the stepped discontinuity to $\lambda/32$. The horn transition and the radiation aperture both generate higher order modes. Therefore, M and N should be determined by the flaring of the transition and the aperture discontinuity. The higher order modes on the aperture contribute more significantly

to the radiation patterns in the back regions. To accurately predict the radiation pattern in the entire region, many more high order modes should be included for this analysis than was in [2, 3]. An empirical formula for determining M and N is

$$(M, N) = \frac{3(A, B)}{\lambda} + 1.5 \quad (27)$$

where A and B represent the size of the horn aperture. To compute the transition more efficiently, only a few modes are needed in the region near the feed and the number of modes should approach (27) as the computation moves toward the horn aperture. This process preserves the accuracy, and reduces the computation time to about one eighth of that which would be required if a constant number of modes determined by (27) are used throughout. When sufficient higher order modes are included, theoretical predictions and measurements are in excellent agreement as presented later in the result section.

C. Thickness of the Aperture Walls

In mid 1960's, Russo, *et. al.*[4] modeled the effect of the aperture wall thickness on the E-plane radiation pattern. During the previous periods of this research program, efforts were also devoted to predict the rapid ripple structures of the H-plane radiation patterns in the back regions. During this research period, we accurately modelled the aperture wall thickness by including a set of roof-top rectangular patch modes around the radiation aperture. This improved model resulted in a much better agreement between the computed and the measured radiation patterns. Discussions of the improvements are included in the next section.

II. RESULTS

A. Modeling Horns with PEC Walls

More extensive comparisons between the measurements and predictions were conducted for the X-band standard gain horn. Table 1 lists measured and predicted antenna parameters for the 20-dB standard gain horn at 9, 10, and 11 GHz, respectively.

Table 1: Computed and measured VSWR's and gains of the standard gain horn

	9 GHz		10 GHz		11 GHz	
	VSWR	Gain	VSWR	Gain	VSWR	Gain
Computed	1.082	19.98dB	1.057	20.63dB	1.031	21.46dB
Measured	1.10	19.72dB	1.06	20.46dB	1.04	21.24dB

Notice that the gains of the standard horn listed in Table 1 have about a constant 0.2 dB differences for all three frequencies. It should be mentioned that the measured gains were obtained using the same horn as the calibration device. Therefore, if there is any inaccuracy in the calibration data, all three data sets are affected. However, the agreement between the computed and measured VSWR's is excellent. Figures 1 to 6 represent the comparisons of the corresponding measured, predicted, and approximated E- and H-plane patterns for the standard gain horn. The approximated patterns are computed using the method outlined in Chapter 12 of *Antenna Theory* by Balanis[5] except that the free space wave impedance in (12.1d) is replaced by the guided wave impedance at the aperture. As demonstrated in the figures, patterns predicted using the moment method code compare much better with the measured patterns for all frequencies in the X-band. The improvements are more evident in the

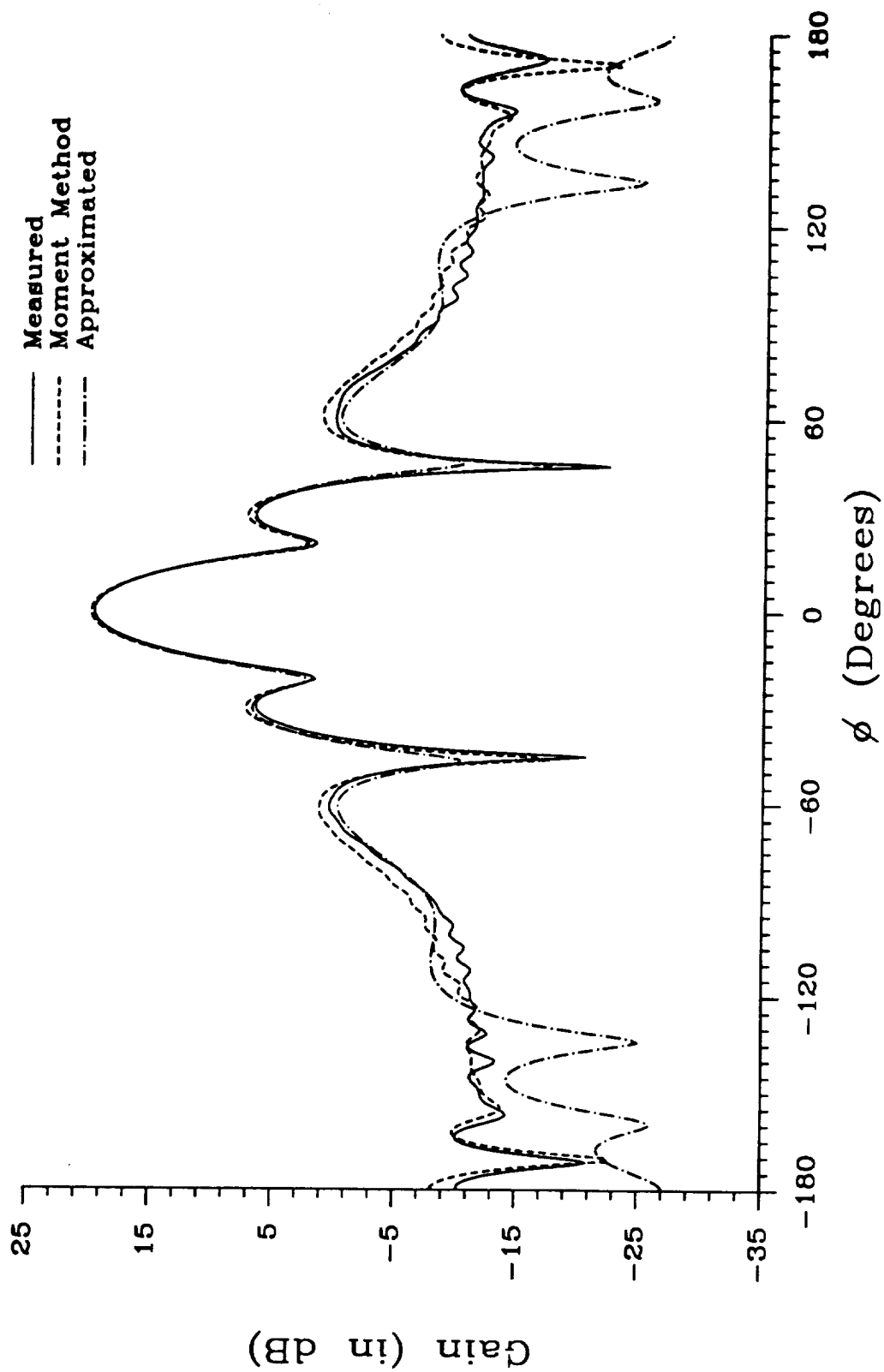


Figure 1. Comparison of E-plane patterns for standard gain horn at 9 GHz.

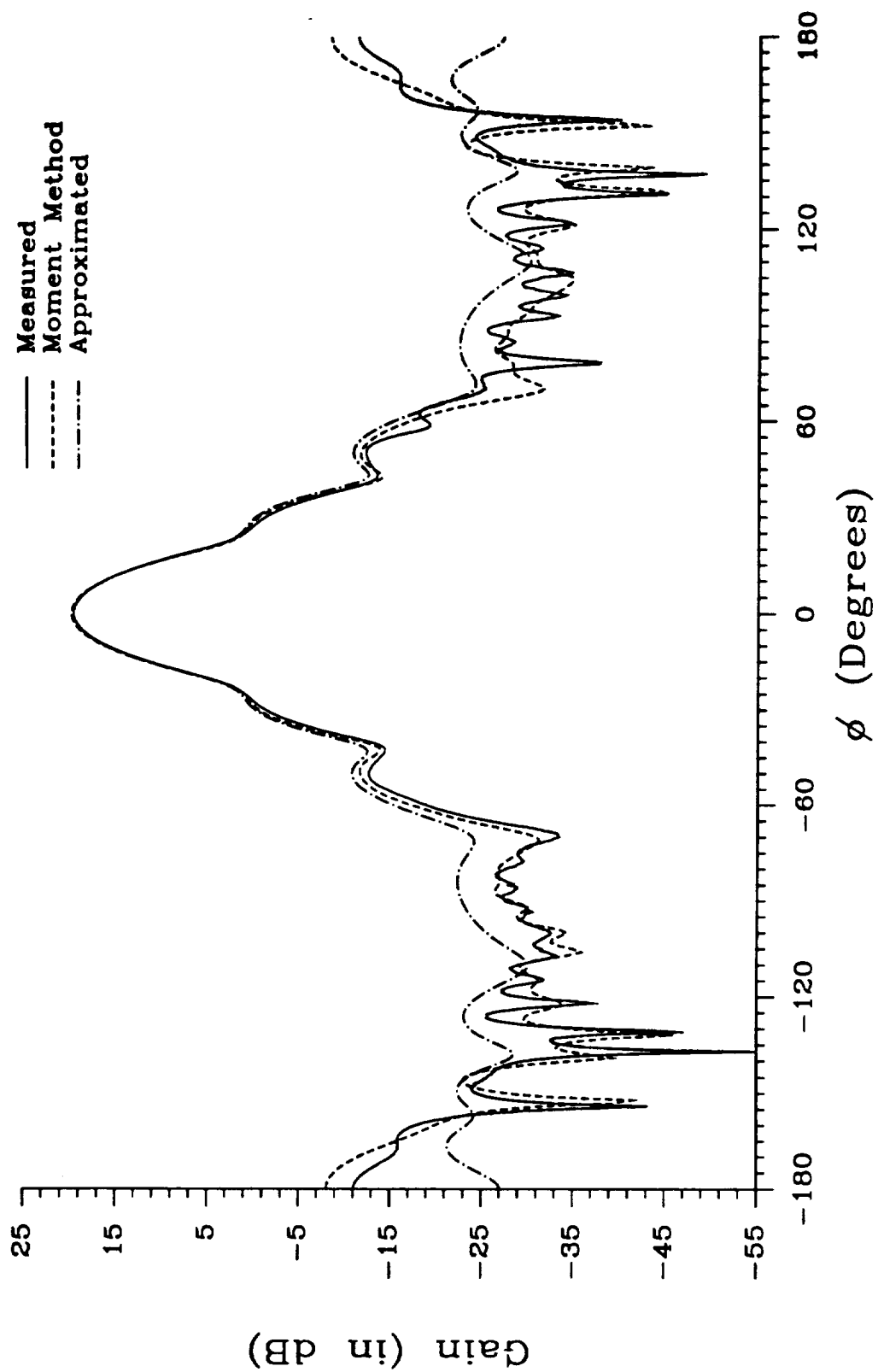


Figure 2. Comparison of H-plane patterns for standard gain horn at 9 GHz.

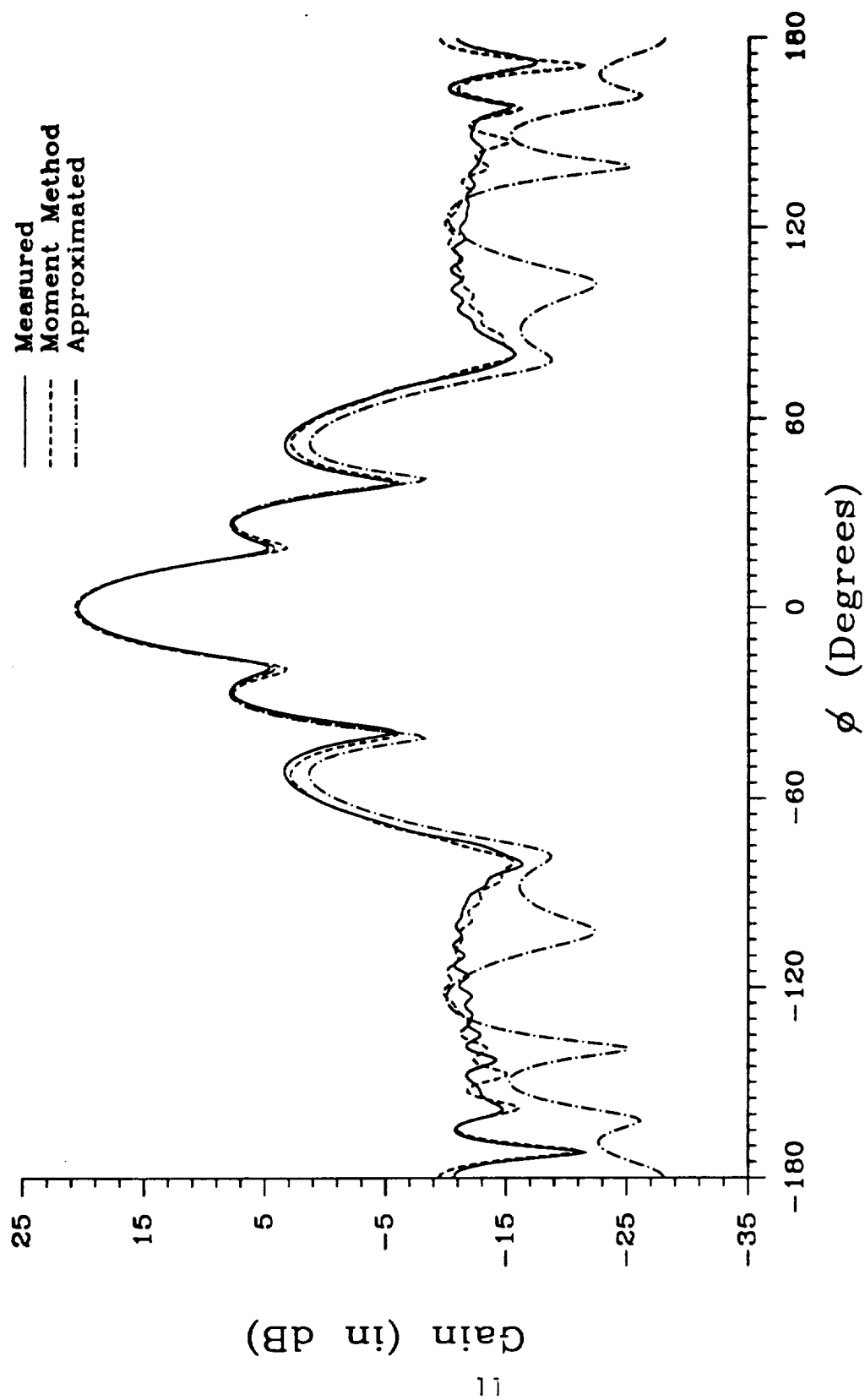


Figure 3. Comparison of E-plane patterns for standard gain horn at 10 GHz.

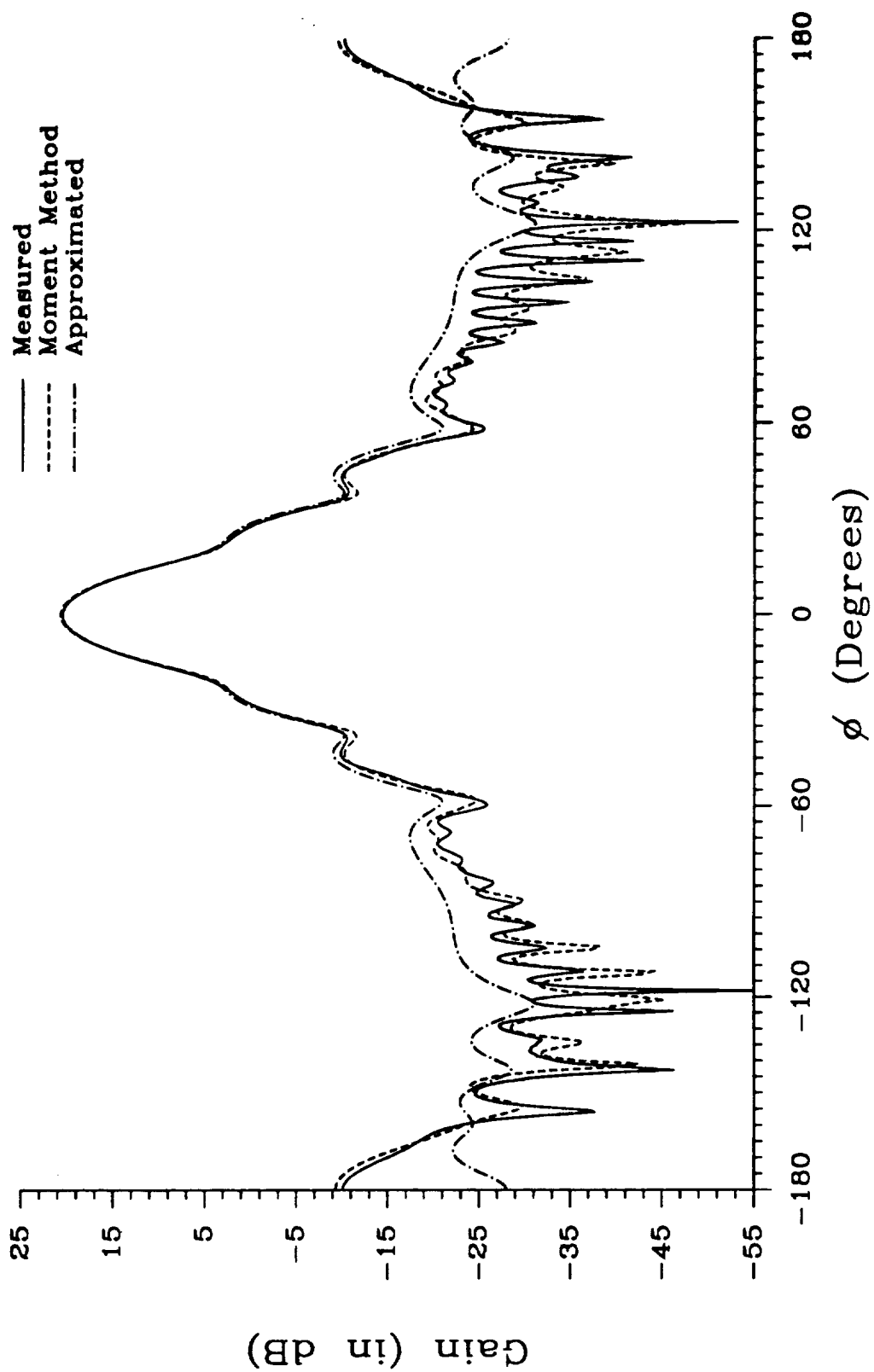


Figure 4. Comparison of H-plane patterns for standard gain horn at 10 GHz.

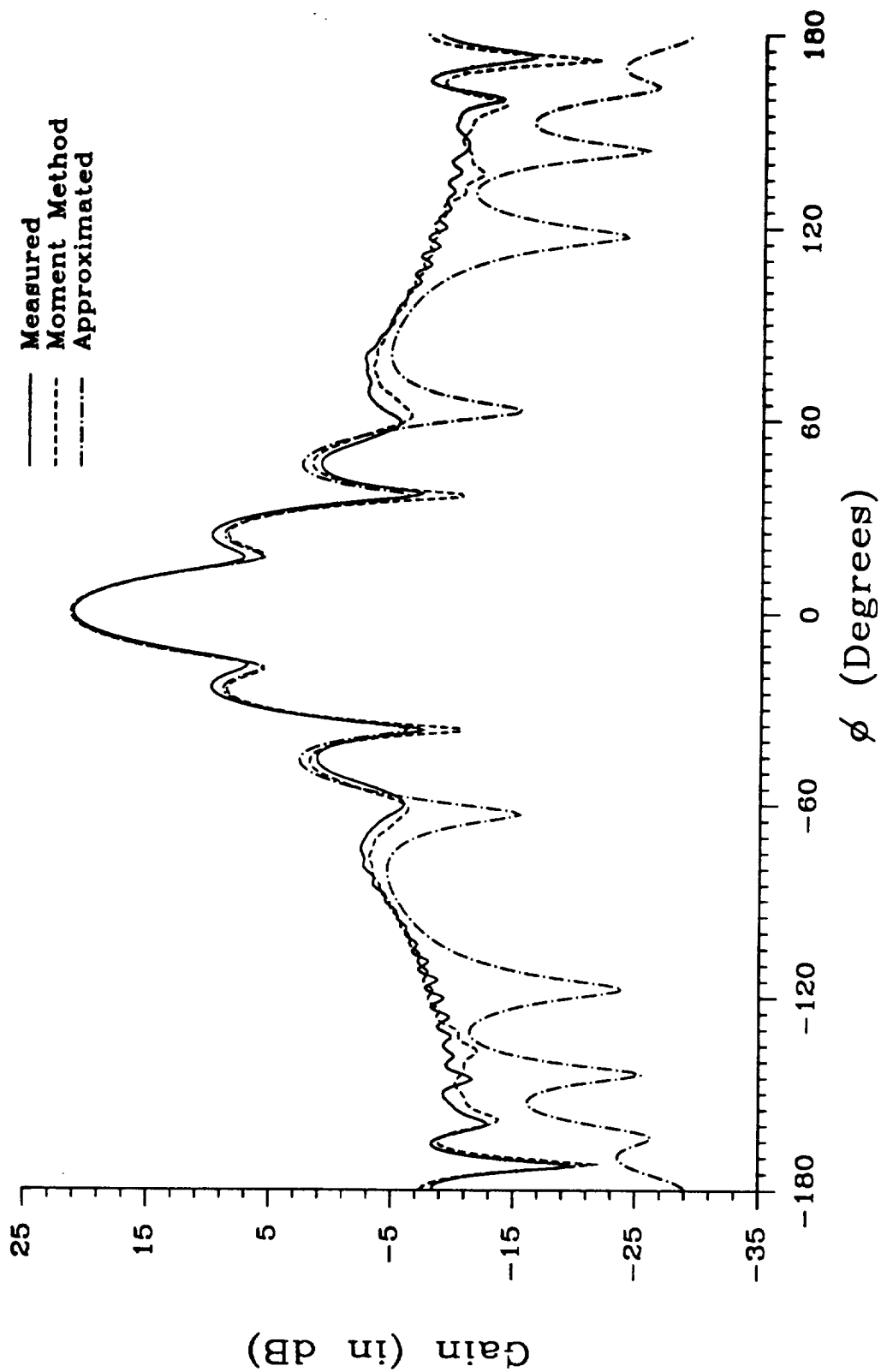


Figure 5. Comparison of E-plane patterns for standard gain horn at 11 GHz.

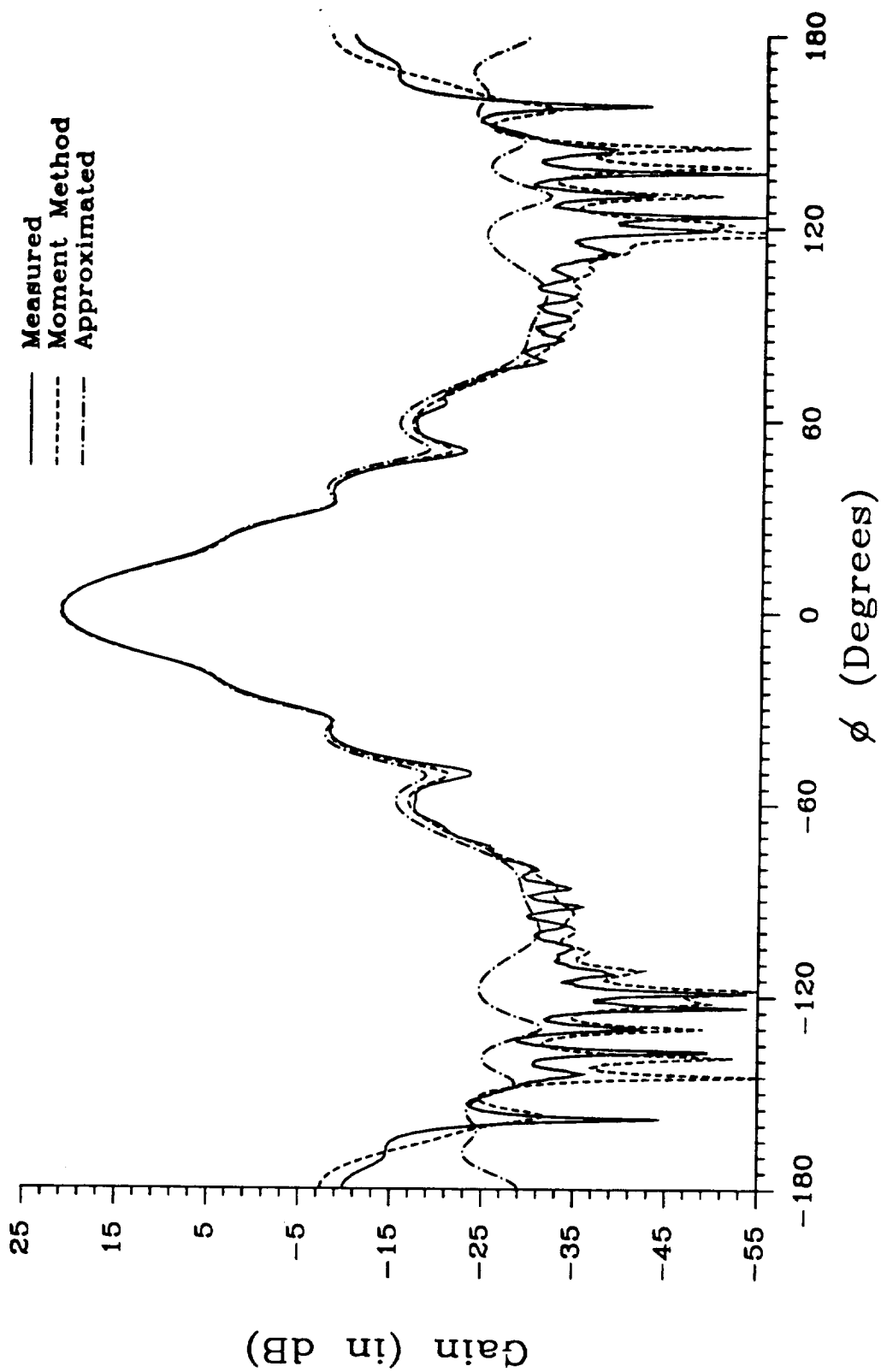


Figure 6. Comparison of H-plane patterns for standard gain horn at 11 GHz.

back regions.

In the previous reporting period, we experienced some difficulties in accurately predicting radiation patterns of large square aperture horns. We also had difficulty in predicting the rapid ripple structures of the H-plane patterns in the back regions. After sufficient number of higher order modes and the thickness of the aperture walls are included in the prediction, these difficulties have been circumvented in this report period. We accurately can model the wall thickness by adding a ring of rectangular roof-top patches around the radiation aperture. In 1965, Russo *et. al.* [4] presented some insignificant changes due to different walls thickness in the analysis of E-plane patterns using GTD. Figures 7 to 12 represent our comparisons of the E- and H-plane patterns of the three horns at 10.0 GHz with and without modeling the aperture wall thickness. Results in the figures agree with Russo's conclusion for the E-plane radiation patterns. However, for the H-plane patterns, the predicted pattern of thin wall model does not agree in the back region with the measured pattern as well as those of the thick wall model. The thick wall model accurately predict the rapid ripple structure in the back region while the thin wall model does not. It is our observation that the rapid ripples of the H-plane pattern are attributed by the wall thickness on the radiation aperture.

The other interesting result obtained in this reporting period is the solution of the aperture field distributions. Figures 13 to 15 represent computed aperture field (E_y and H_x components) distributions of the standard gain horn at 9, 10, and 11 GHz. Contrary to the classical beliefs that the aperture fields are basically TE_{10} with parabolic phase fronts, distributions presented here demonstrate much more complicated aperture field distributions. The deviations from the approximated aperture distributions are more evident for H_x . Figures 16 and 17 represent aperture field

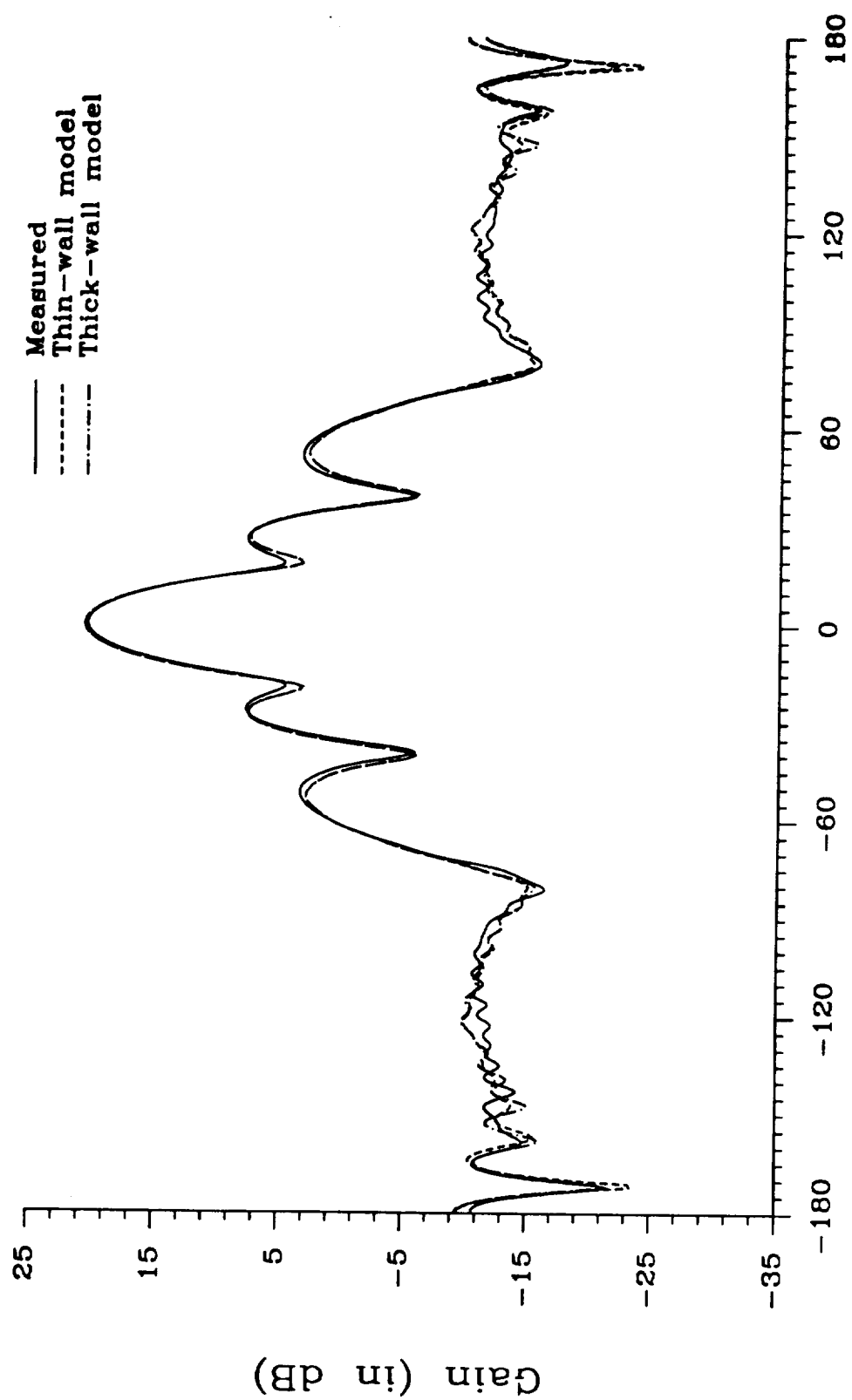


Figure 7. Comparison of E-plane patterns for different aperture wall models of standard gain horn at 10 GHz.

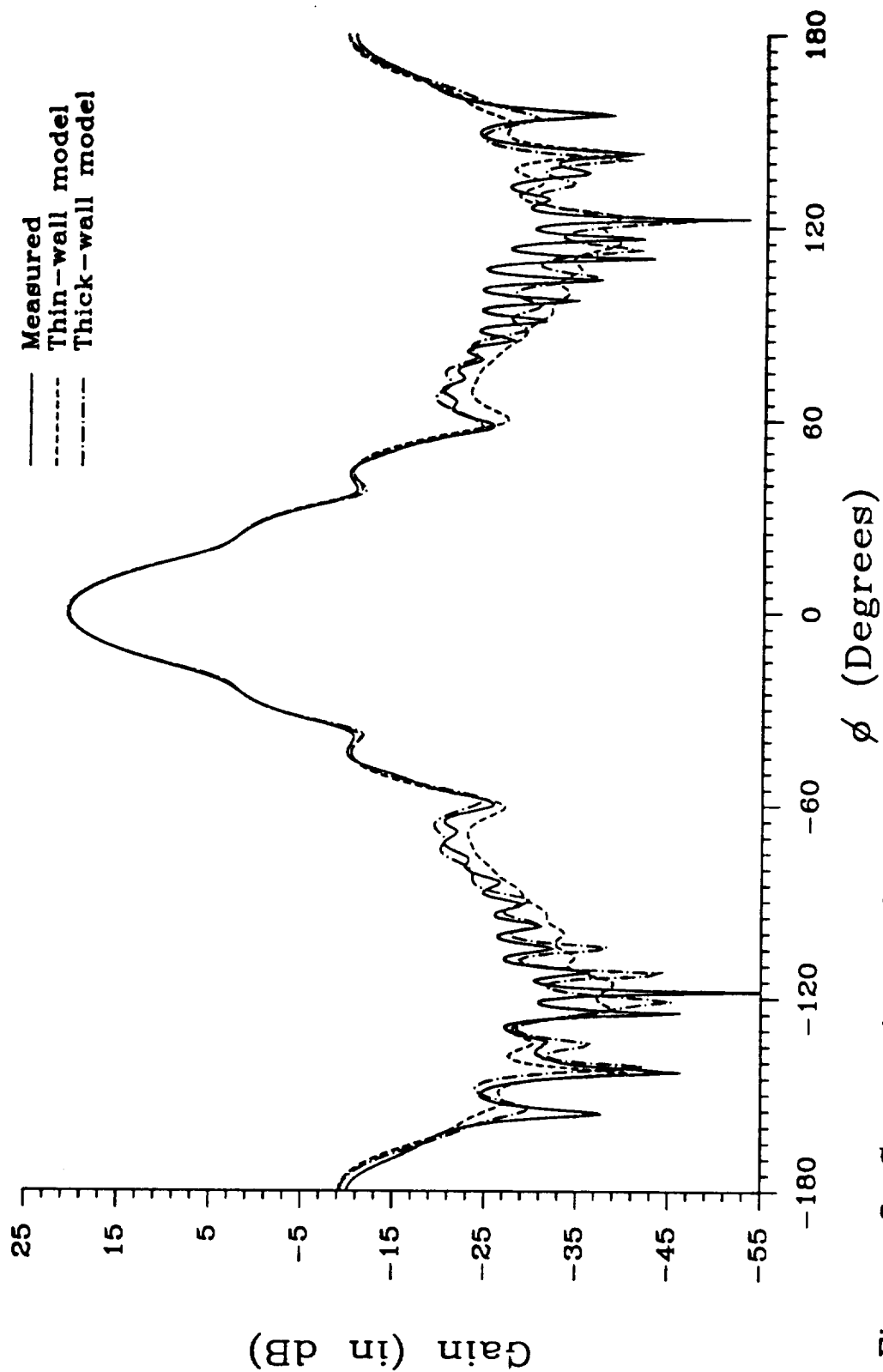


Figure 8. Comparison of H-plane patterns for different aperture wall models of standard gain horn at 10 GHz.

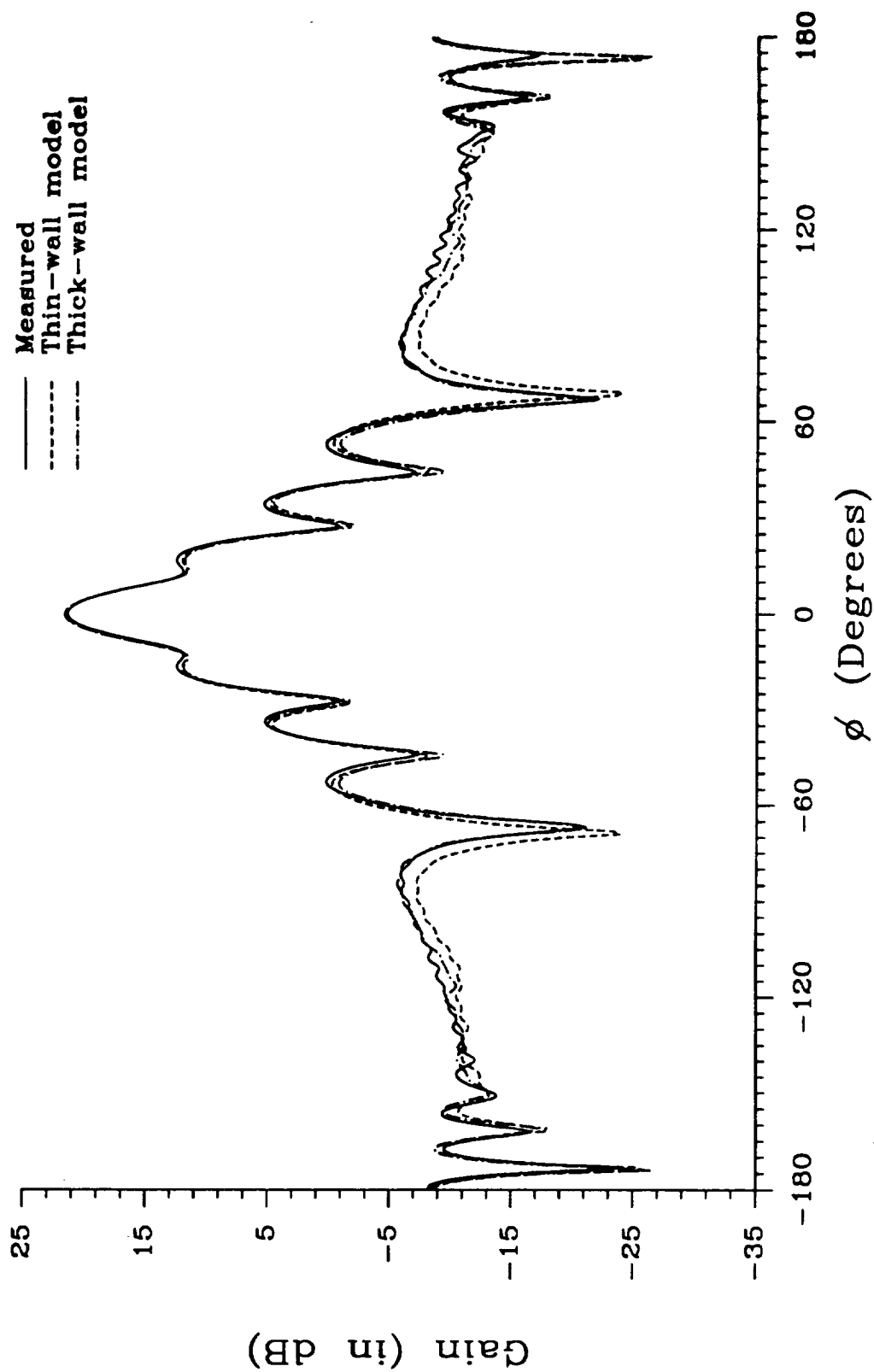


Figure 9. Comparison of E-plane patterns for different aperture wall models of 5-inch square horn at 10 GHz.

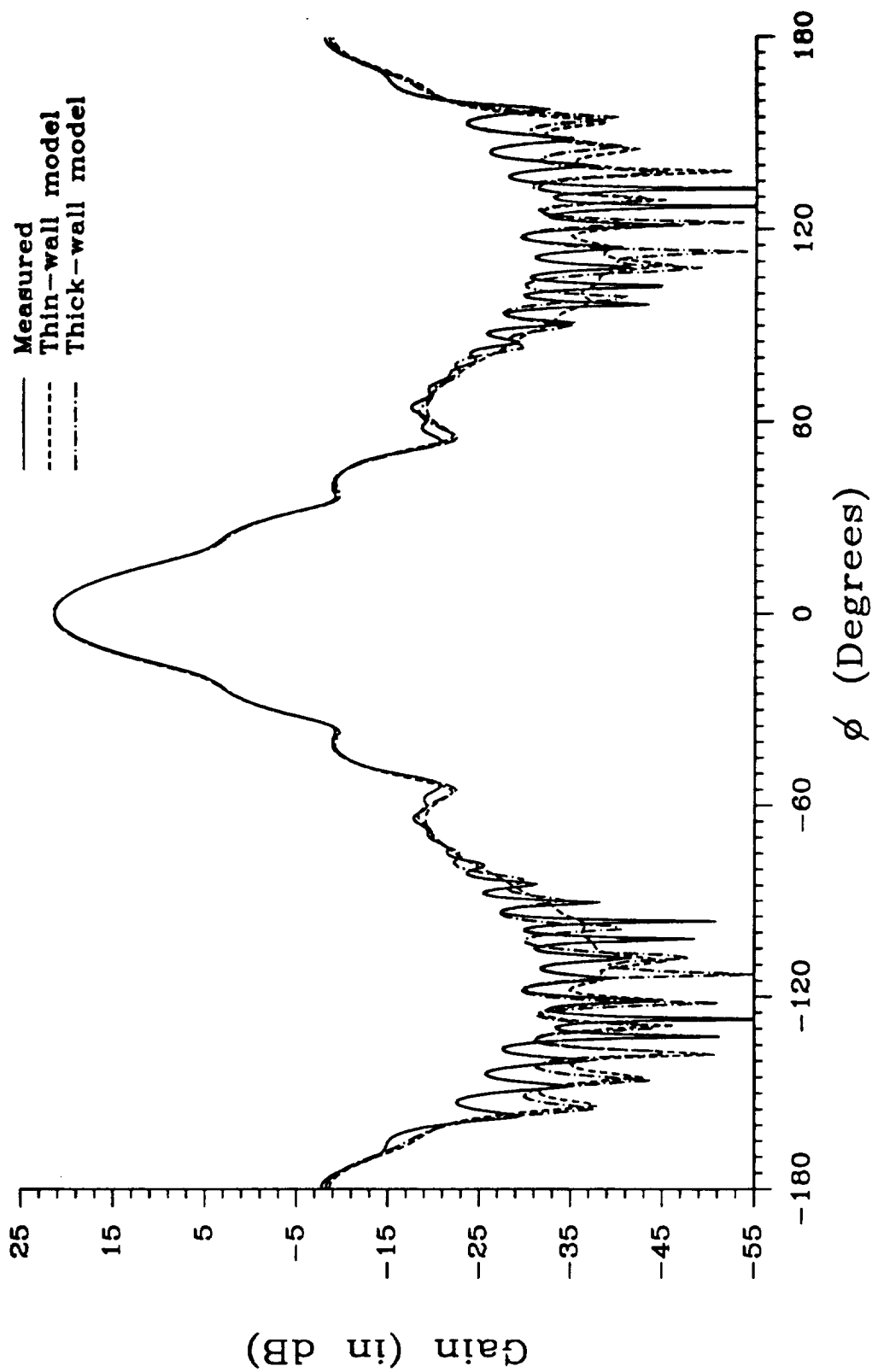


Figure 10. Comparison of H-plane patterns for different aperture wall models of 5-inch square horn at 10 GHz.

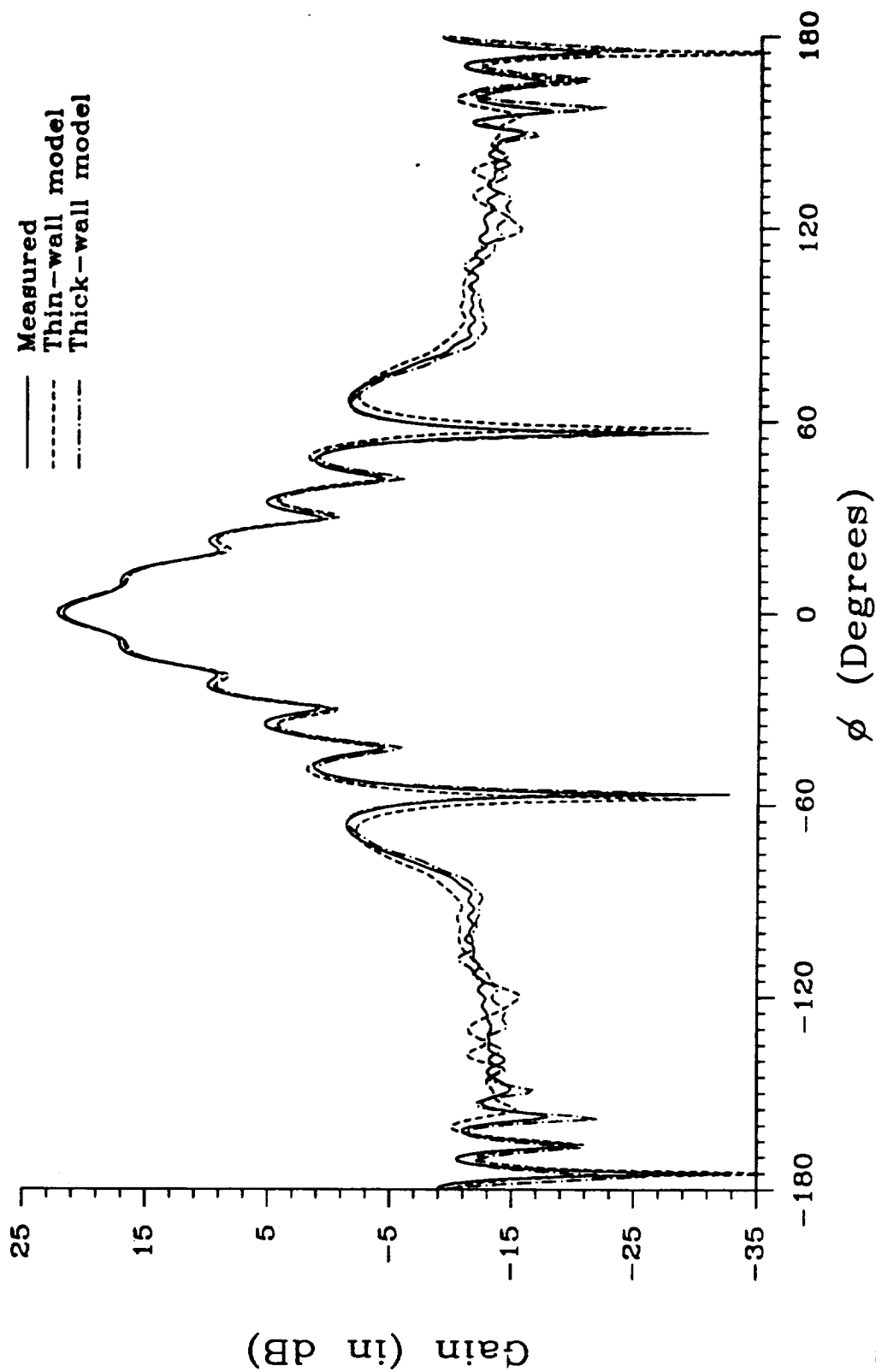


Figure 11. Comparison of E-plane patterns for different aperture wall models of 7-inch square horn at 10 GHz.

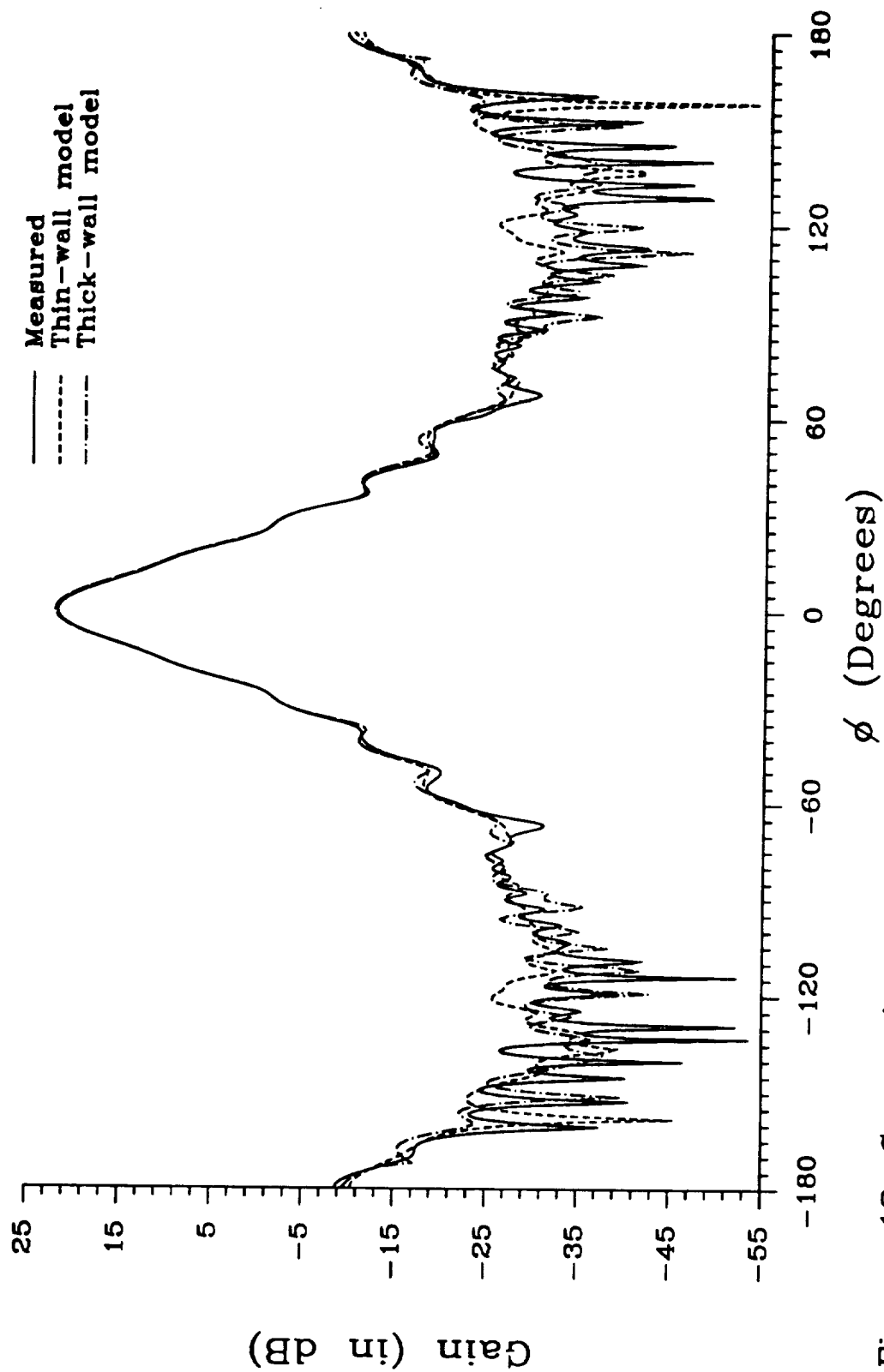


Figure 12. Comparison of E-plane patterns for different aperture wall models of 7-inch square horn at 10 GHz.

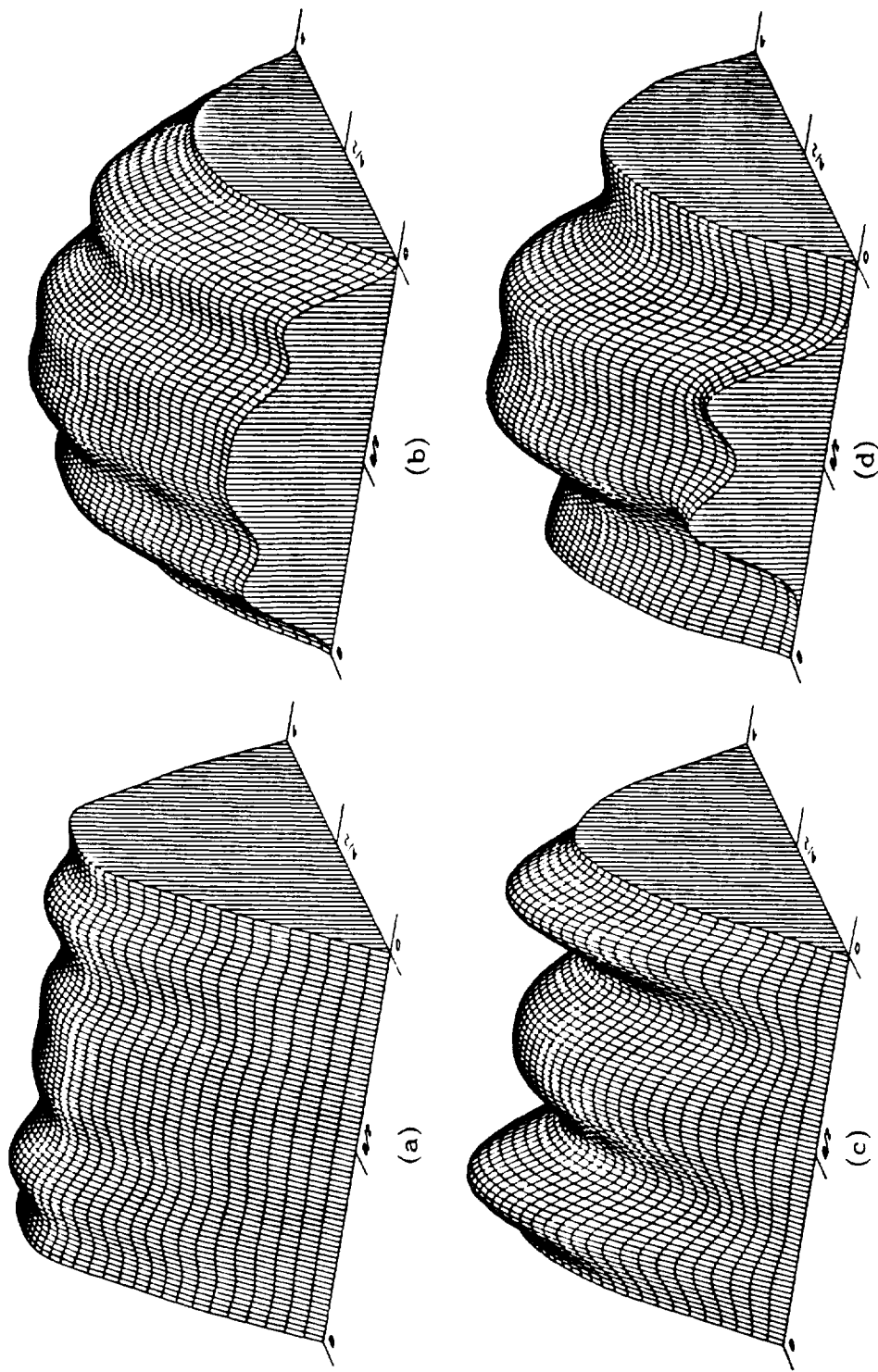


Figure 13. Aperture fields of X-Band standard horn at 9 GHz.
 (a), (b)---Magnitude and phase distributions of E ,
 (c), (d)---Magnitude and phase distributions of H_x .

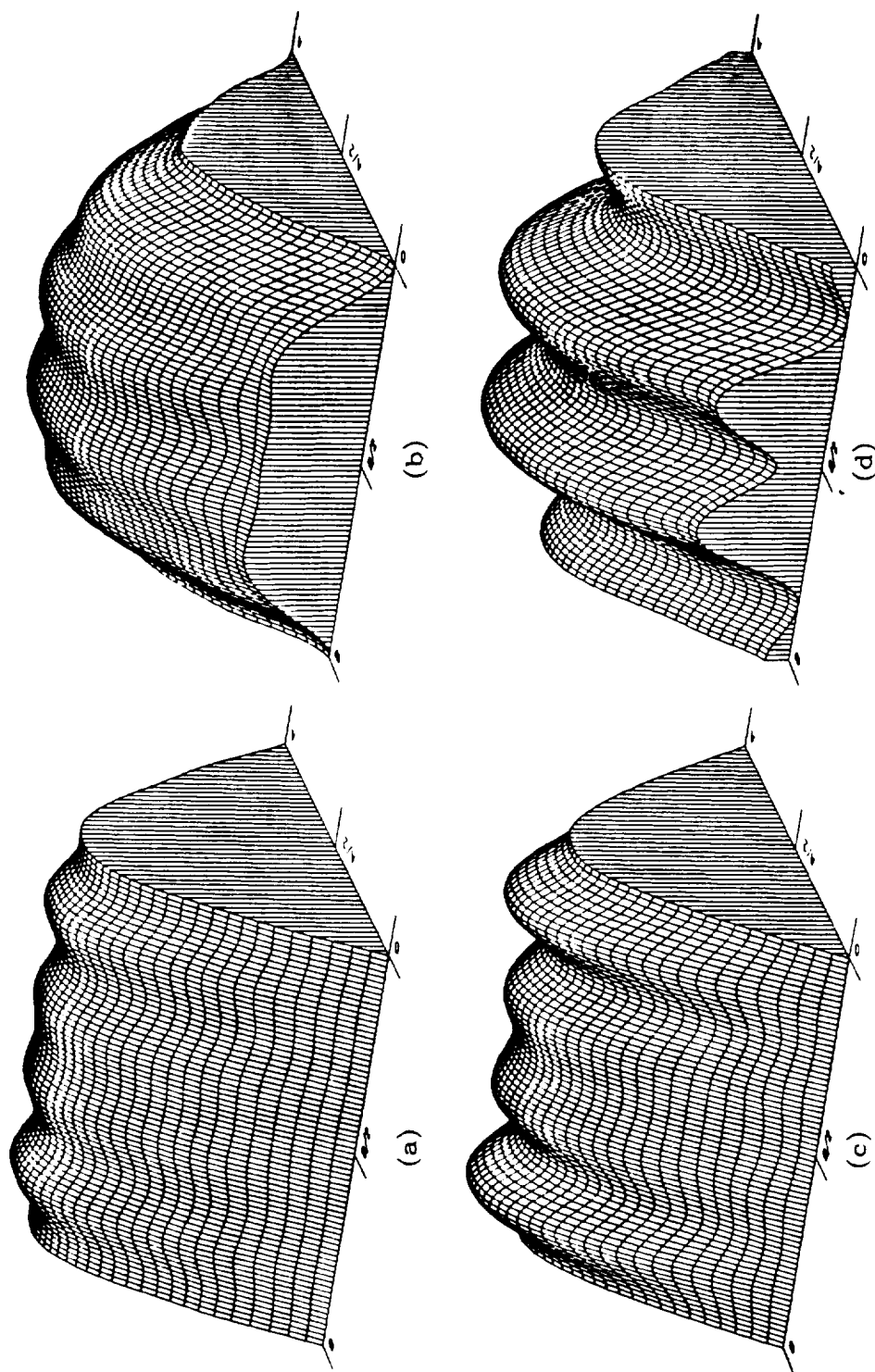


Figure 14. Aperture fields of X-Band standard horn at 10 GHz.

(a), (b) --- Magnitude and phase distributions of E ,
(c), (d) --- Magnitude and phase distributions of H_x .

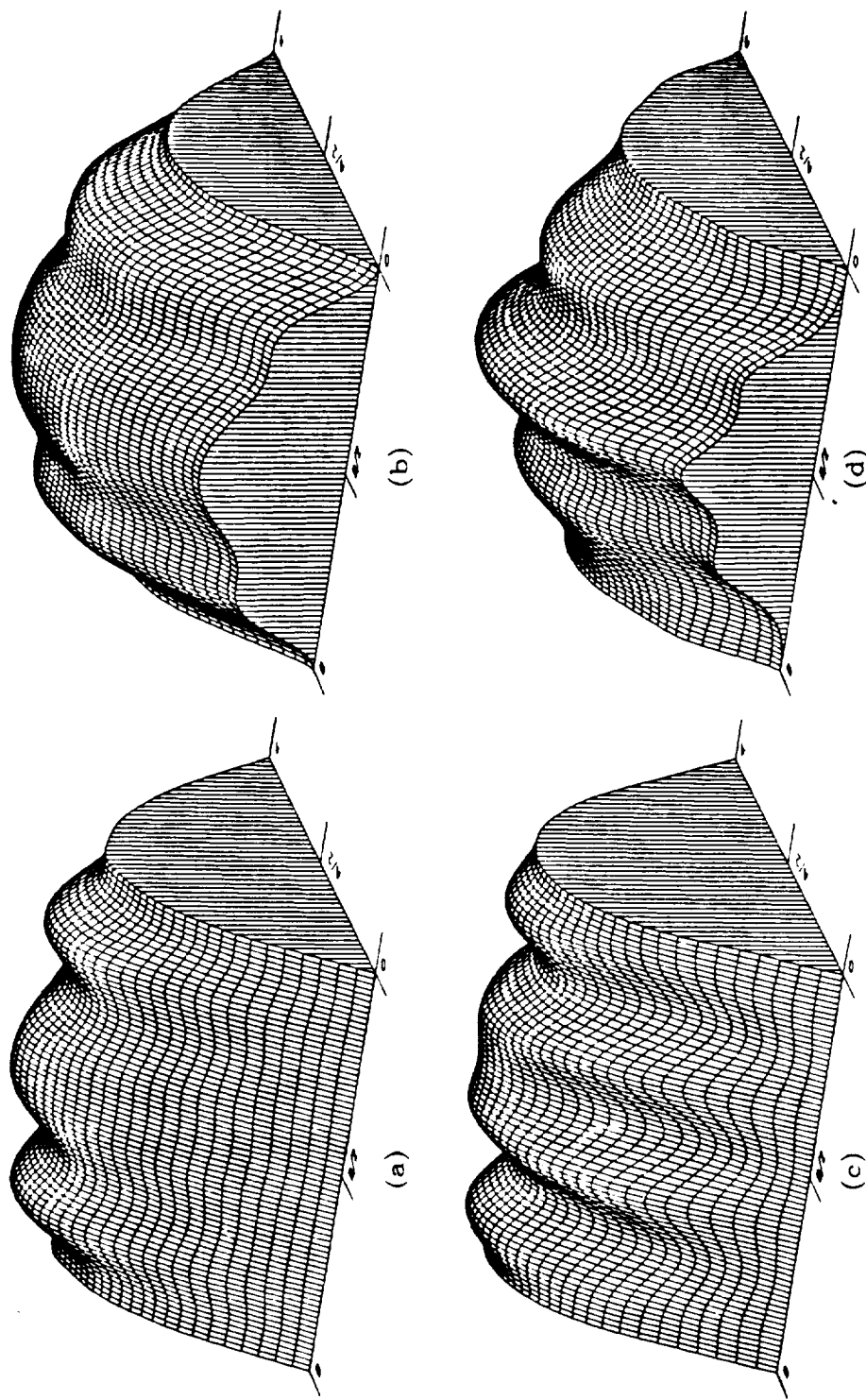


Figure 15. Aperture fields of X-Band standard horn at 11 GHz.

(a), (b) --- Magnitude and phase distributions of E_y ,
 (c), (d) --- Magnitude and phase distributions of H_x .

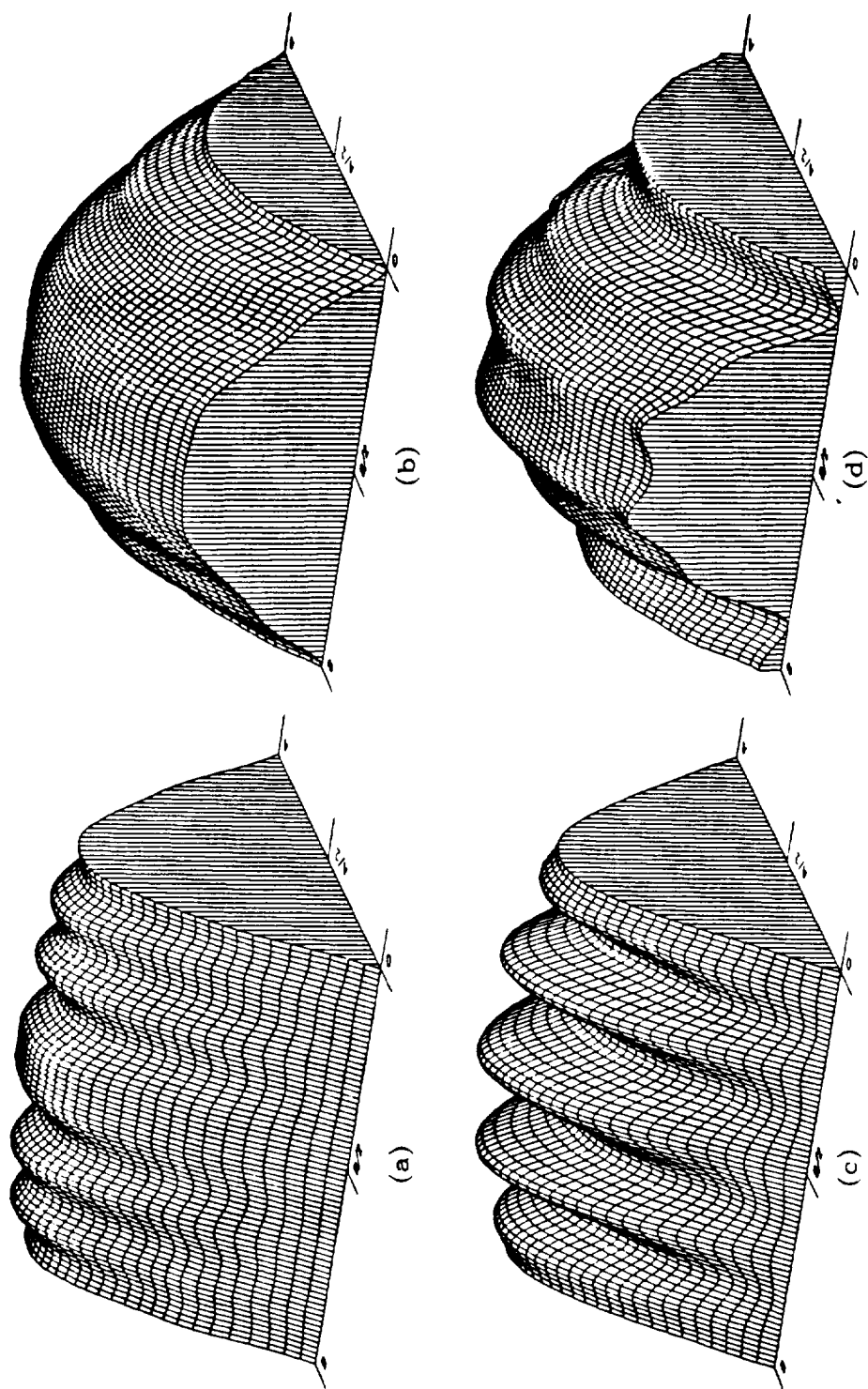


Figure 16. Aperture fields of 5-inch square horn at 10 GHz.

(a), (b) — Magnitude and phase distributions of E ,
(c), (d) — Magnitude and phase distributions of H_x

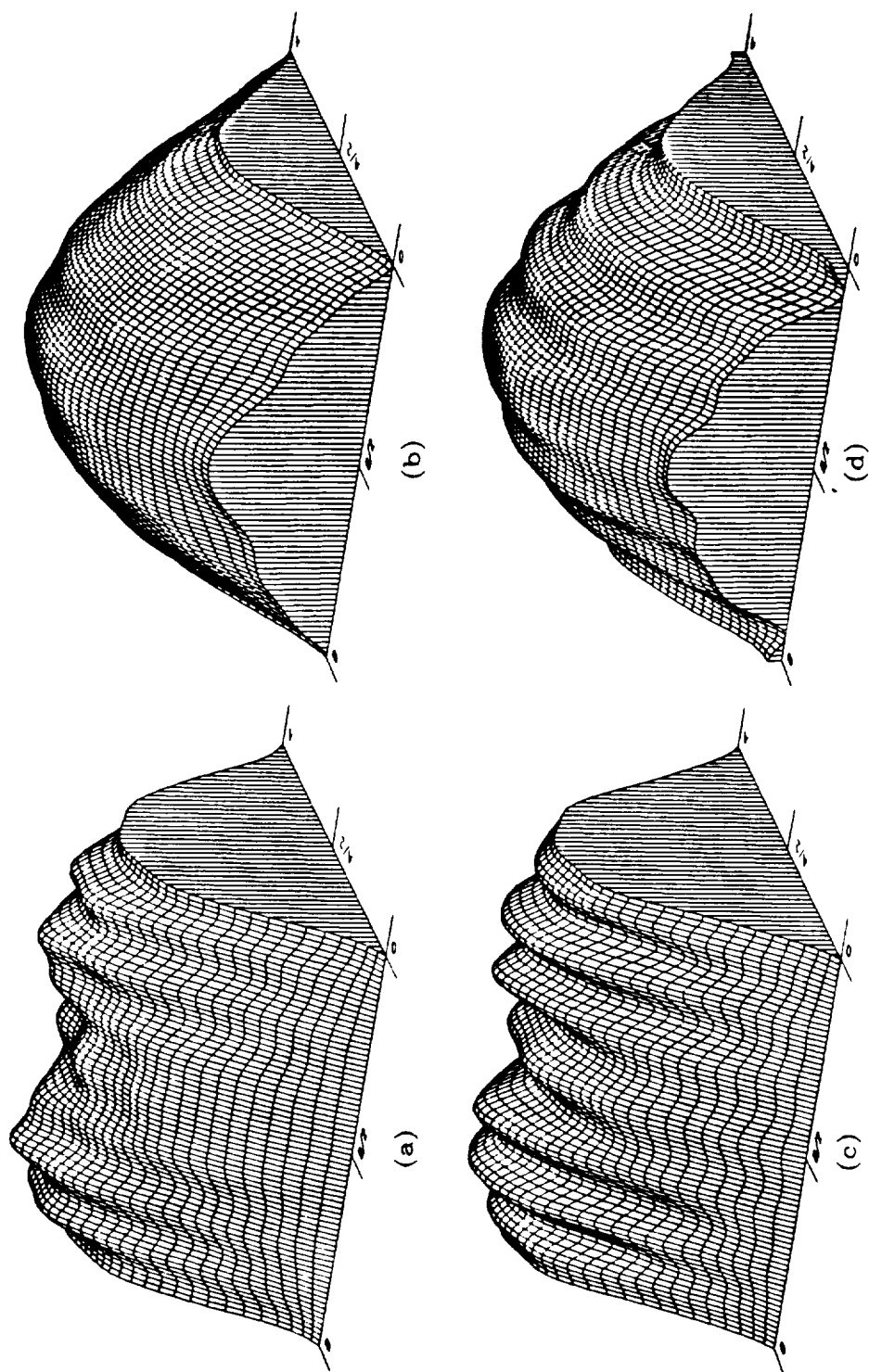


Figure 17. Aperture fields of 7-inch square horn at 10 GHz.

(a), (b) --- Magnitude and phase distributions of E_z ,

(c), (d) --- Magnitude and phase distributions of H_x .

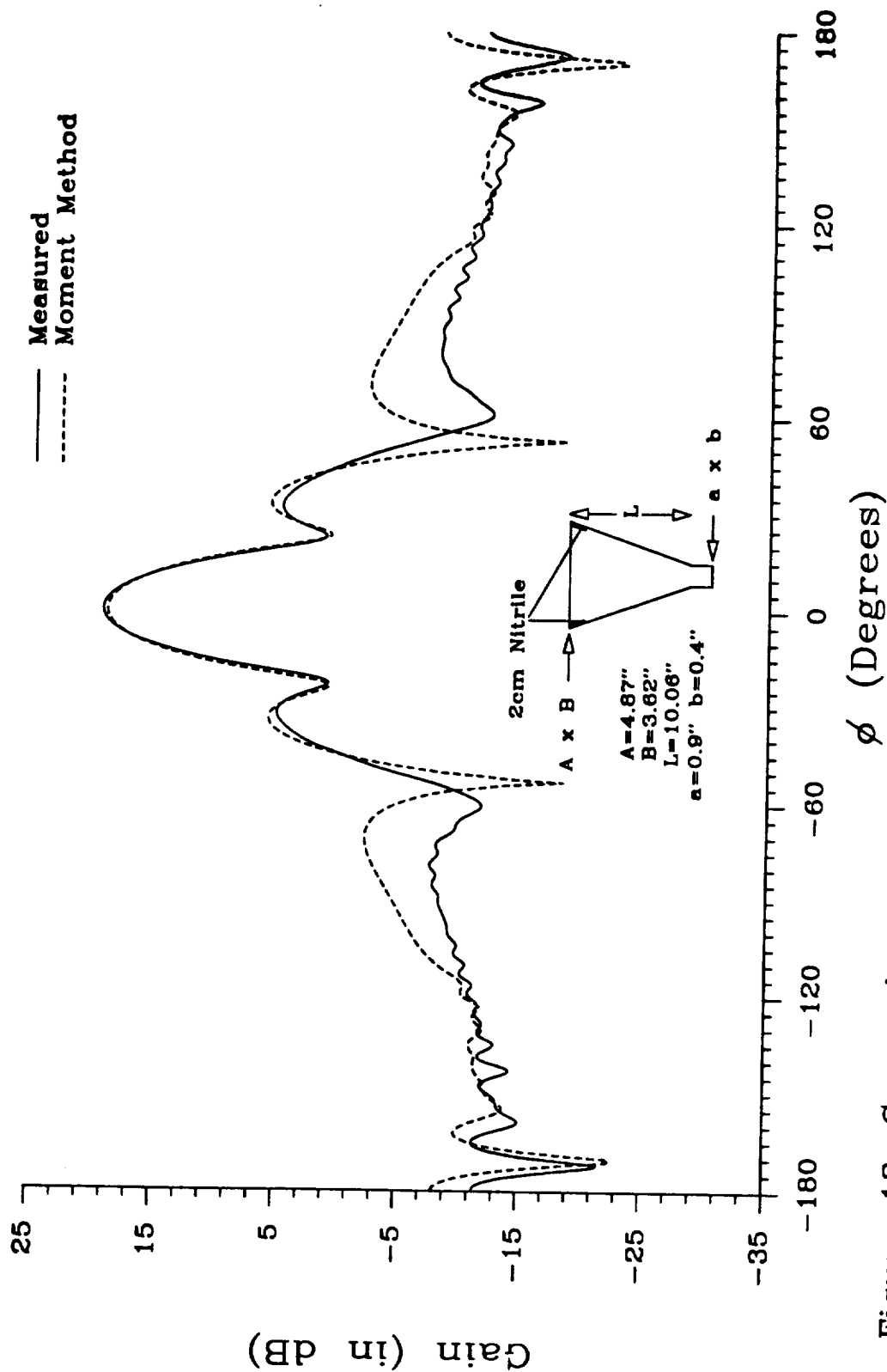


Figure 18. Comparison of E-plane patterns for standard gain horn at 10 GHz with 2cm of lossy Nitrile material coating.

distributions of the 5-inch and 7-inch square horns at 10 GHz. Figures 13 to 17 also demonstrate that as the electrical sizes of the aperture become larger, amplitude distributions of the aperture field become more complicated; however, phase distributions approach a parabolic phase front.

B. Modeling Horns with Impedance Walls

Figure 18 represents the comparison of E-plane patterns at 10 GHz for the standard gain horn coated with 2-cm of Nitrile material on the E-plane walls near the radiation aperture. This preliminary result has some discrepancies in the sidelobe regions. We believe it is due to the incompleteness of the full-wave analysis of the field distribution in the coated section of the horn. As a result of this inaccuracy, the predicted gain is 0.4 dB lower than the measured gain. In the next reporting period, we will concentrate our effort on resolving this problem.

III. DISCUSSIONS

The full-wave and integral equation method code were applied to analyze electrically large pyramidal horn antennas with or without lossy material coating on inner walls of the horn. For the analysis of the pyramidal horn antenna with perfectly conducting walls, accurate prediction can be achieved by:

- include sufficient higher order modes in the full-wave analysis. The required number of modes can be determined using the empirical formula of (27).
- limit the size of the stepped discontinuity to less than $\lambda/32$ in the stepped-waveguide modeling of the continuous horn transition.

- limit the largest segment size of the roof-top patch to less than 0.2λ to ensure an effective and accurate solution of the electric field integral equation on the outer surfaces of the pyramidal horn antenna.
- include the aperture thickness in the segmentation of the outer surface.

When these rules are observed, the moment method code can be used to predict the pyramidal horn with excellent accuracy. For a horn antenna with lossy impedance inner wall, the solution for the outside surface is the same as that of the perfectly conducting case. A full-wave representation of the field configuration in the coated section of the horn is needed to accurately include the effect of the lossy material coating.

IV. FUTURE WORK

In the coming reporting period, the research will be focused on accurately modeling of horn antennas with material coatings on the inner walls. Algorithms on stabilizing the eigen value of the partially lossy material coated waveguides will be introduced to ensure the accuracy of the eigen mode representation of the field structure inside the coated section of the horn. When such a modeling is completed, the synthesis techniques are going to be implemented and compared with measurements.

V. PUBLICATIONS

During this reporting period, one paper has been submitted for publication in the IEEE Transaction on Antennas and Propagations. One paper was submitted and accepted as one of the finalists for student paper contest in the plenary session of the *1992 IEEE APS/URSI/NEM Joint Symposia*. The papers to be published or presented are all under the sponsorship of the NASA-AVRADA Joint Research Program Research Program Office research grant No. NAG-1-1183.

1. Kefeng Liu, C. A. Balanis and G. C. Barber, "Analysis of pyramidal horn antennas using moment methods," submitted for publication in *IEEE Trans. on Antennas and Propogat.*
2. Kefeng Liu, and C. A. Balanis, "Integral equation analysis of high-gain pyramidal horn antennas," selected as one of the finalists for presentation in *1992 IEEE APS/URSI/NEM Joint Symposia*, for student paper contest.

References

- [1] C. A. Balanis, *Advanced Engineering Electromagnetics*. Wiley, 1989.
- [2] J. A. Encinar and J. M. Rebollar, "A hybrid technique for analyzing corrugated and noncorrugated rectangular horns," *IEEE Trans. Antennas Propagat.*, vol. AP-34, pp. 961–968, Aug. 1986.
- [3] T. Wriedt, K. H. Wolff, F. Arndt, and U. Tucholke, "Rigorous hybrid field theoretic design of stepped rectangular waveguide mode converters including the horn transitions into half-space," *IEEE Trans. Antennas Propagat.*, vol. AP-37, pp. 780–790, June 1989.
- [4] P. M. Russo, R. C. Rudduck, and L. J. Peters, "A method for computing e-plane patterns of horn antennas," *IEEE Trans. Antennas Propagat.*, vol. AP-13, pp. 219–224, Mar. 1965.
- [5] C. A. Balanis, *Antenna Theory Analysis and Design*. Wiley, 1982.